Inverse Problems in Science and Engineering
Vol. 00, No. 00, January 2011, 1–24

RESEARCH ARTICLE

A Comparison of Extended Kalman Filter, Ultrasound Time-of-Flight Measurement Models for Heating Source Localisation

M.R. Myers[a] *, A.B. Jorge[b], M.J. Mutton[c], and D.G. Walker[a] **

[a]Department of Mechanical Engineering, Vanderbilt University, Nashville, TN, 37235, USA;
[b]Mechanical Engineering Institute, Federal University of Itajubá, Itajubá, MG, Brazil;
[c]Industrial Measurement Systems, Inc., 2760 Beverly Drive, Suite 4, Aurora, IL 60502

(*Received 00 Month 200x; in final form 00 Month 200x*)

Comparisons of six heating source localisation measurement models are conducted where temperature or ultrasonic time of flight readings provide the measurement update to the extended Kalman filter for estimating the location of a high heat flux spot source on a flat plate. For a particular measurement model, one of two processes are used: 1) directly using the measurements as the measurement vector in the extended Kalman filter or 2) indirectly obtaining the distance from the sensor to the heating source based on the measurement and then using the obtained distance as the measurement vector in the extended Kalman filter. For the direct models, the Jacobian required by the extended Kalman filter is obtained numerically using finite differences from the finite element forward conduction solution. For the indirect models, the derivatives of the distances with respect to the state variables are obtained in closed form. Heating source localisation results and convergence behaviour are compared for the six measurement models investigated. The ellipse from ultrasonic pulse one-way time of flight measurement model produces the best results when considering accuracy of converged solution, ability to converge to the correct solution given different initial guesses, and smoothness of convergence behaviour. Additionally, extended Kalman filter, extended information filter, and least squares inverse methods are compared for a parameter identification to quantify the heat flux (q'') and convection coefficient (h) on the plate. All three inversion methods produce similar results which is significant as future work will consider only the extended Kalman filter.

Keywords: ultrasound; ultrasonic; Kalman filter; heat source; localisation

AMS Subject Classification: 80A20; 80A23; 65C20

1. Introduction

Locating a transient, concentrated heating source on a thin solid surface has applications in the manufacturing and aerospace industries. In many of these applications, the location of the heating source cannot be directly observed. Measurements can be performed of some other phenomenon, such as surface temperatures, which can be related to heating source location through a forward conduction solution. The heating source location can then be estimated using a suitable inverse approach. This work details such a solution with motivation coming from the aerospace industry where air flowing across a hypersonic (Mach 5+) vehicle

*Corresponding author. Email: Mike.Myers@Vanderbilt.Edu

**Principal corresponding author. Email: Greg.Walker@Vanderbilt.Edu

ISSN: 1741-5977 print/ISSN 1741-5985 online

DOI: 10.1080/1741597YYxxxxxxxx
http://www.informaworld.com

body transitions from laminar flow to turbulent flow. Knowledge of the transition region can provide numerous benefits to air vehicle design, thermal protection system design, and air vehicle in-flight control [1]. The heat flux in the turbulent region after the transition is significantly higher than in the laminar region ahead of the transition [2–5]. We propose a novel measurement system incorporating ultrasonic thermometry and an inverse method based on the extended Kalman filter [6] that could be used to locate the boundary layer transition region. In the foregoing analysis, we have simplified the problem to study a laboratory scale spot heating scenario. Ultimately, if we can prove the inversion method, measurement model, and heating parameter estimates on this problem, then we will have confidence in transitioning our techniques to hypersonic conditions. Several measurement strategies have been studied for similar applications including using thermocouples [7], thermopiles [8], thin-film temperature gauges [9], optical sensors coupled with thermographic phosphors [10, 11], infrared sensors [12], and ultrasonic transducers. Ultrasonic thermometry techniques are effective for gases, fluids, and solids [13–15] and have been used with success in many process control systems [16, 17] and non-destructive evaluation applications [18–20]. Kalman filters assume all beliefs and disturbances are Gaussian and are built on a framework of predicting the state based on an input to the system and correcting the predicted state based on sensor observations [21, 22].

This work compares six heating source localisation measurement models. These comparisons are needed to determine which measurement model should be incorporated into future work and determine if ultrasonic transducers can outperform thermocouples for heating source localisation. These measurement models represent different ways to collect measurements and different ways to process the data. Two measurement models are based on thermocouple sensors and four models are based on ultrasonic transducer sensors. Comparison of the six measurement models is performed using the extended Kalman filter and we analyse the convergence behaviour of each model. For a particular measurement model, one of two processes are used: 1) directly using the measurements as the measurement vector in the extended Kalman filter or 2) indirectly obtaining the distance from sensor to the heating source based on the measurement and then using the obtained distance as the measurement vector in the extended Kalman filter.

This work also compares the extended Kalman filter, extended information filter, and least squares for parameter identification of boundary conditions for an experiment involving a concentrated high heat flux spot source. Previous work [23] covered the experiment and the parameter identification, however this work extends previous work by detailing the comparison of extended Kalman filter, extended information filter, and least squares. In addition to determining unknown boundary conditions for the experiment, the comparison serves to validate our choice of the extended Kalman filter for heating source localisation. Convergence behaviour and computational resources are used in evaluating the three methods.

2. Flat Plate Experiment

The flat plate experiment and data used in this work is identical to the experiment described and analysed for a different problem in previous work [23]. The experiment discussion is repeated here for the reader's convenience. This work concentrates first on a large flat plate heated over a small area with a known heat source. Consider a 61 cm x 30.5 cm x 0.635 cm stainless steel 316L plate (Figure 1) with constant properties (Table 1). The plate is sized large enough such that the plate edges do not affect the temperature profile in the plate during the experi-

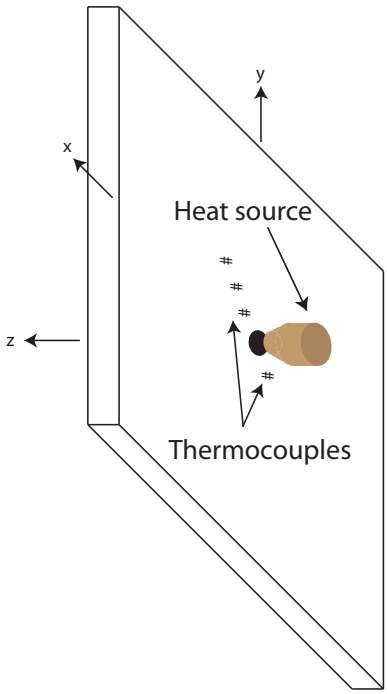

Figure 1. Illustration of flat plate with heat source and sensors (not drawn to scale) [23].

Table 1. Material properties for the stainless steel 316L test sample used in the conduction experiments.

Property	Value
density (ρ)	$8,000\,\mathrm{kg/m^3}$
thermal conductivity (k)	$14.6\,\mathrm{W/m\,K}$
specific heat (c_p)	$500\,\mathrm{J/kg\,K}$
sound speed (v_0)	$5,100\,\mathrm{m/s}$ @ 293 K
ultrasonic TOF temperature factor (ξ)	$110 \times 10^{-6}\,1/\,\mathrm{K}$
sample length	61 cm
sample width	30.5 cm
sample height	0.635 cm

ment. Four K-type thermocouples were attached on one side and four on the other. With plate centre being the origin and the x-axis being the length (Figure 1), thermocouples were attached at (x, y) locations of (1 cm, 1 cm), (2 cm, 2 cm), (3 cm, 3 cm), and (-1 cm, -1 cm) on the heated side ($z = 0$) and on the non-heated side (z=0.635cm). The desire was to have thermocouple pairs in exactly the same position on either side of the plate allowing measurement of the temperature difference between the two sides. The thermocouples were secured to the plate with thermal grease and Kapton tape to ensure good thermal contact. Flat black paint was applied to a 1.5 cm diameter area at the plate centre to maximise energy absorption from the heater. The plate was oriented vertically with the positive y-axis pointing up. A Research, Inc. SpotIR 4150 heater with focusing cone was positioned approximately 2 mm from the plate surface such that its beam struck the plate centre. Experiments were conducted with the heater running at full-power which, according to manufacturer's specifications, produces $1.7\,\mathrm{MW/m^2}$ of heat flux on the plate in a circular area 0.635 cm in diameter. Consequently, approximately 54 Watts of energy are being absorbed by the plate when the heater is on.

During the experiment, the heater is turned on at $t = 300$ s and turned off and removed at $t = 600$ s. Data acquisition equipment was used to record thermocouple

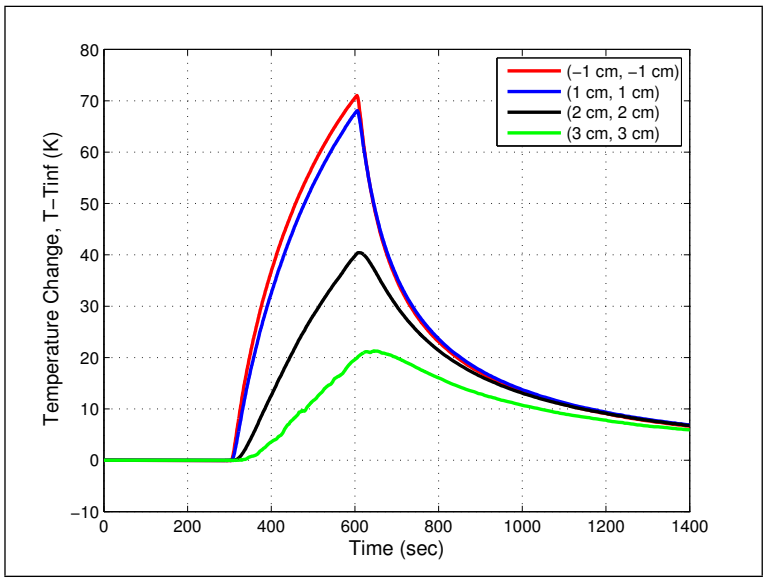

Figure 2. Temperature response on non-heated side of the plate at four sensor locations [23].

temperature readings every second during the experiment. A MIKRON Thermo Scan TS7302 infrared camera was used to collect thermal images of the plate and heater. Coupled with a laptop computer, this system recorded thermal images every five seconds during the experiment. Benefits gained from the thermal images include visualization of the temperature distribution throughout the experiment and the need to model secondary convection and radiation heating in addition to modeling the primary high heat flux coming from the heater's beam. Figure 2 illustrates the thermocouple temperature data recorded during the experiment. Analysis of the data indicates that a spatial temperature gradient of 6 °C/mm exists during heating in the area of the thermocouple sets closest to the source [(1 cm, 1 cm) and (−1 cm, −1 cm)]. Positioning the heating source and the sensors within this degree of precision proved difficult. Therefore, sensor and heating source placement error is the most likely cause of the discrepancies between the two thermocouple sets closest to the source.

3. Forward Conduction Solution

The forward conduction solution used in this study was described and analysed for a different problem in previous work [23] and is repeated here for the reader's convenience. The forward conduction solution leverages COMSOL Multiphysics® by the COMSOL Group and MATLAB® by The Mathworks, Inc. The COMSOL® model uses a finite element mesh with smaller elements near the heat source and larger elements near the plate edges to conserve computing resources.

For the flat plate detailed in Section 2, the governing equation for the subdomain (conduction in the plate) is

$$\rho C_p \frac{\partial T}{\partial t} - \nabla \cdot (k \nabla T) = Q \tag{1}$$

where ∇ is the Laplacian, and Q is an internal heat source (0 in this case).

For the flat plate, k is assumed constant. Thus, the subdomain governing equation

is

$$\nabla^2 T = \frac{\rho C_p}{k}\frac{\partial T}{\partial t} \tag{2}$$

or

$$\frac{\partial^2 T}{\partial x^2} + \frac{\partial^2 T}{\partial y^2} + \frac{\partial^2 T}{\partial z^2} = \frac{\rho C_p}{k}\frac{\partial T}{\partial t} \tag{3}$$

The boundary condition is

$$n \cdot (k\nabla T) = q_0 + h(T_{inf} - T) \tag{4}$$

where n is the surface normal vector, q_0 is the inward heat flux.

The first meshing method analyzed in this work is the 3D free mesh using tetrahedral elements. A 0.635 cm diameter cylindrical subdomain in the plate's center was used to create a boundary for applying the heating source. This technique also creates small elements near the heating source and large elements far away from the source where temperature gradients are small thereby conserving computing resources. Mesh refinement was accomplished using all of the predefined free mesh sizes available in COMSOL® starting with the coarsest mesh and proceeding to the finest mesh. Grid convergence was achieved with 13,256 elements and 26,628 degrees of freedom, however the solution does not agree with an analytical solution of heating through a circular domain without convection [24] as illustrated in Figure 3. Element sizes from the converged 3D free mesh were used to create an extruded mesh which does agree the analytic solution (Figure 3). The extruded mesh was generated by first creating 2D triangle elements in the plate's $x-y$ plane and then extruding the 2D mesh in the z-direction to create prism elements. Two subdomains consisting of a 0.635 cm diameter circle with a maximum element size of $1e-3$ m and a 6 cm diameter circle with a maximum element size of $5e-3$ m were used. The 2D mesh was created with the predefined normal free mesh setting in COMSOL®. The mesh extrusion process incorporates an option to create multiple mesh layers, therefore grid independence is contingent upon the number of layers through the thickness of the plate. The worst case is where the highest temperature gradients through the plate's thickness exist which is located at plate center. Figure 4 illustrates the computed temperature profile through the plate at plate center with one, two, four, and six mesh layers. The grid convergence study led to the selection of three mesh layers through the plate's thickness dimension, 9,780 total elements, and 45,983 degrees of freedom. Agreement between the final COMSOL® solution and the closed-form solution [24] is acceptable with mean absolute error less than 0.5 K.

4. Parameter Identification

Even with manufacturer specifications, the heat transfer between the radiative heater and the plate is not known with much certainty. Further complicating matters, the heater's proximity to the plate implies an unknown amount of secondary radiation and convection heating on the plate. The focusing cone reaches temperatures in excess of 200 °C and the lamp is cooled with forced air that exits the heater through the focusing cone pointed at the plate. Figure 5 illustrates the boundary conditions used in modeling the plate. For this initial analysis, the main heat flux and convection coefficient are estimated. The secondary heating is modelled with a

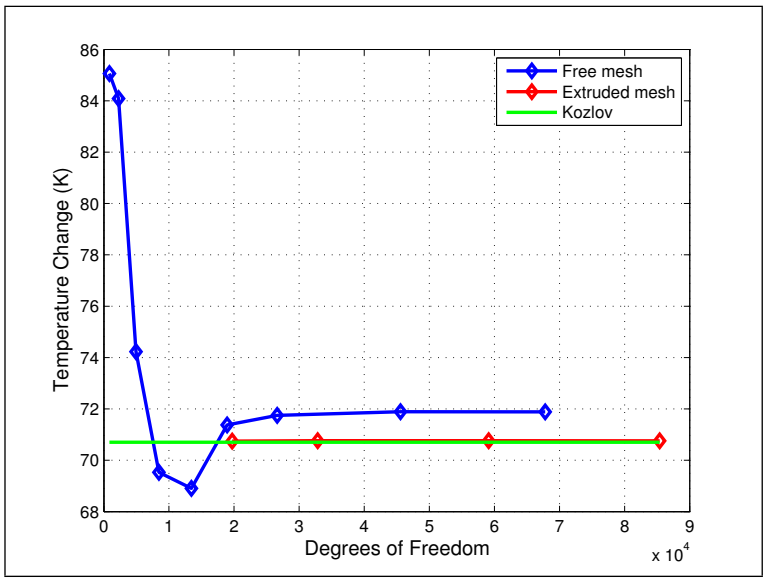

Figure 3. Grid independence results for the heated side at 1.4cm from the source and $t = 400\,\mathrm{s}$.

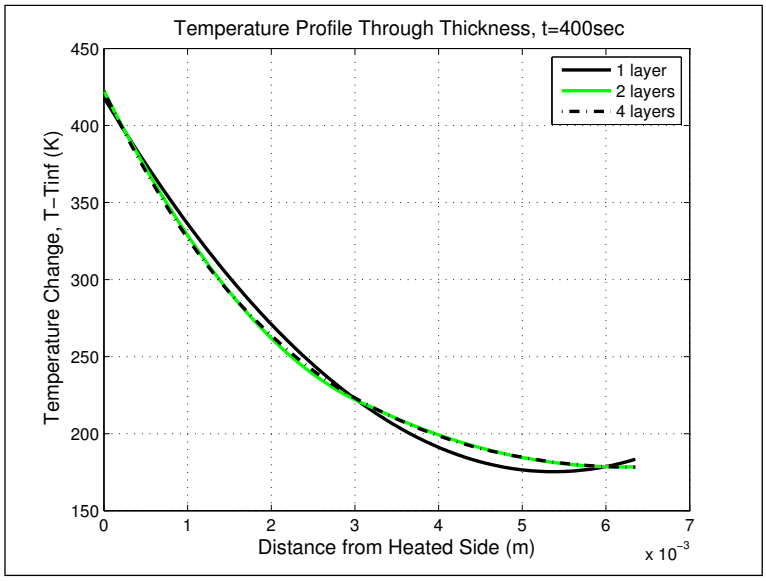

Figure 4. Number of mesh layers for best accuracy.

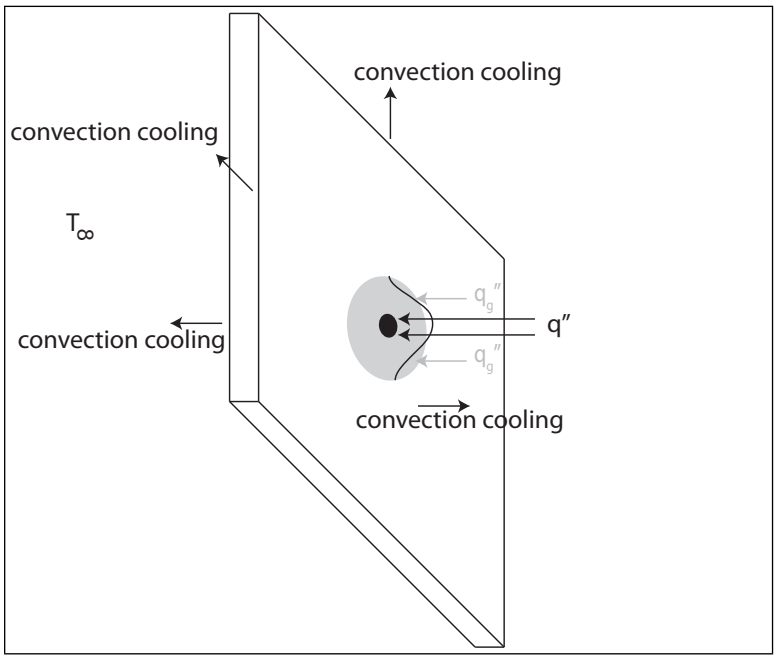

Figure 5. Illustration of boundary conditions on the flat plate.

Gaussian profile of $q''_g = 100\,\mathrm{W/m^2}$ and $\sigma_g^2 = 0.0009\,\mathrm{m^2}$. The convection coefficient being estimated is the average value over the duration of the experiment. While areas of the heated side of the plate may have a different convection coefficient value during heating, once the heater is removed, the average convection coefficient is identical on both sides of the plate. Thus, the heat transfer coefficient h is assumed constant and identical on both sides of the plate. Estimating h using free convection correlations [25] produces an expected range of $2\,\mathrm{W/m^2K} \leq h \leq 5\,\mathrm{W/m^2K}$. Since the plate edges do not contribute significantly to the thermal load, $h = 3\,\mathrm{W/m^2K}$ is assumed on all four plate edges.

Three inverse methods are compared to quantify the heat flux (q'') and convection coefficient (h) on the plate: least squares, extended Kalman filter, and extended information filter. The extended Kalman filter and extended information filter are members of a family of recursive state estimators, collectively called Gaussian filters [6]. The extended information filter is the information form of the Kalman filter. Both filters linearise nonlinear Gaussian systems. For the inversion, the entire experiment is treated as one event and temperature measurements are combined together. The experiment covers 1,400 seconds and data was recorded at one second intervals. Not all of the data is needed for the inverse and longer time steps can be used during periods of little thermal activity. Accordingly, one measurement at $t = 0\,\mathrm{s}$, one measurement per second from $t = 290$ to $800\,\mathrm{s}$ (the heater is on from $t = 300$ to $600\,\mathrm{s}$), and one measurement per five seconds from $t = 805$ to $1,400\,\mathrm{s}$ was used. The 5,056 temperature measurements therefore are effectively 5,056 separate sensors. All three methods start with an initial guess of the state $x_0 = [q\ h]^{\mathrm{T}} = [1.7\,\mathrm{MW/m^2}\ 5.0\,\mathrm{W/m^2K}]^{\mathrm{T}}$ and are processed recursively to convergence.

The least squares estimator is $x_{new} = x + (X_\beta^{\mathrm{T}} X_\beta)^{-1} X_\beta^{\mathrm{T}} (Y - T|_x)$ where X is the Jacobian based on finite differences obtained from COMSOL® by independently varying the state parameters 0.1%, Y are the experimentally obtained temperatures, and $T|_x$ are temperatures based on current estimates for the state x [26]. The Jacobian was normalised to produce a better conditioned matrix. The algorithm for the extended Kalman filter is listed in Table 2 where $\overline{X}_t$ is the predicted state,

Table 2. Extended Kalman filter algorithm.

Step	Operation
1	$\overline{X}_t = a(U_t, X_{t-1})$
2	$\overline{\Sigma}_t = A_t \Sigma_{t-1} A_t^T + Q_t$
3	$K_t = \overline{\Sigma}_t B_t^T (B_t \overline{\Sigma}_t B_t^T + R_t)^{-1}$
4	$X_t = \overline{X}_t + K_t(Z_t - b(\overline{X}_t))$
5	$\Sigma_t = (I - K_t B_t)\overline{\Sigma}_t$
6	Return to step 1 if solution not converged

Table 3. Extended information filter algorithm.

Step	Operation
1	$X_{t-1} = \Omega_{t-1}^{-1} \phi_{t-1}$
2	$\overline{\Omega}_t = (A \Omega_{t-1}^{-1} A^T + Q)^{-1}$
3	$\overline{\phi}_t = \overline{\Omega}_t a(U_t, X_{t-1})$
4	$\overline{X}_t = a(U_t, X_{t-1})$
5	$\Omega_t = \overline{\Omega}_t + B^T R^{-1} B$
6	$\phi_t = \overline{\phi}_t + B R^{-1} [Z_t - b(\overline{X}_t) + B \overline{X}_t]$
7	Return to step 1 if solution not converged

$a(U_t, X_{t-1})$ is the state model based on the input U_t and the previous state X_{t-1}, A is the state Jacobian, $\overline{\Sigma}$ is the uncertainty estimate, Q_t is the state covariance, K_t is the Kalman gain, B_t is the measurement Jacobian, R_t is the measurement covariance, $b(\overline{X}_t)$ is the measurement transition function and represents the predicted measurements from the forward conduction solution based on the predicted state, and Z_t represents the actual measurements. The filter represents the belief at time t by the state X_t and the covariance Σ_t. For the flat plate considered here, there is no input to the state thus the state model is $a = I_2$ and the state Jacobian is $A = I_2$, where I_2 is a 2×2 identity matrix. The measurement transition function b is a $5,056 \times 1$ matrix of the predicted temperatures from the forward conduction solution, and the measurement Jacobian B is obtained using finite differences (a $5,056 \times 2$ matrix) by independently varying the state parameters 0.1%. The state covariance matrix Q is a 2×2 diagonal matrix using $\sigma_q^2 = 0.1\,\mathrm{MW}^2/\mathrm{m}^4$ and $\sigma_h^2 = 0.1\,\mathrm{W}^2/\mathrm{m}^4\mathrm{K}^2$. These values were chosen to achieve smooth convergence behaviour since small values for the state covariance matrix cause the Gaussian filters to diverge while arbitrarily large values for the state covariance matrix render the Gaussian filters essentially identical to the least squares method. The thermocouples have a measurement accuracy of $\pm 1.5\,^\circ\mathrm{C}$, which translates to a measurement variance of $\sigma_T^2 = 0.25\,^\circ\mathrm{C}^2$. This value was used for the diagonal elements of the measurement covariance matrix R, a $5,056 \times 5,056$ matrix. The filter is initialised with the initial state x_0 (stated above) and covariance $\Sigma_0 = 0$. For the extended information filter (Table 3), a, A, b, B, R, and Q are identical to those in the extended Kalman filter. The extended information filter possesses an advantage of allowing the inverse of the measurement covariance matrix Q^{-1} to be computed once and reused for all iterations. Because the initial state covariance matrix Σ_0 is inverted in the extended information filter, the filter was initialised with $\Sigma_0 = R$ instead of the zero matrix used to initialise the extended Kalman filter.

Figures 6 and 7 illustrate the convergence behaviour for all three methods. The extended Kalman filter and extended information filter converge identically and are presented together. The Gaussian filters converge a bit slower than the least squares method, however the convergence is smoother. Once convergence was achieved, sta-

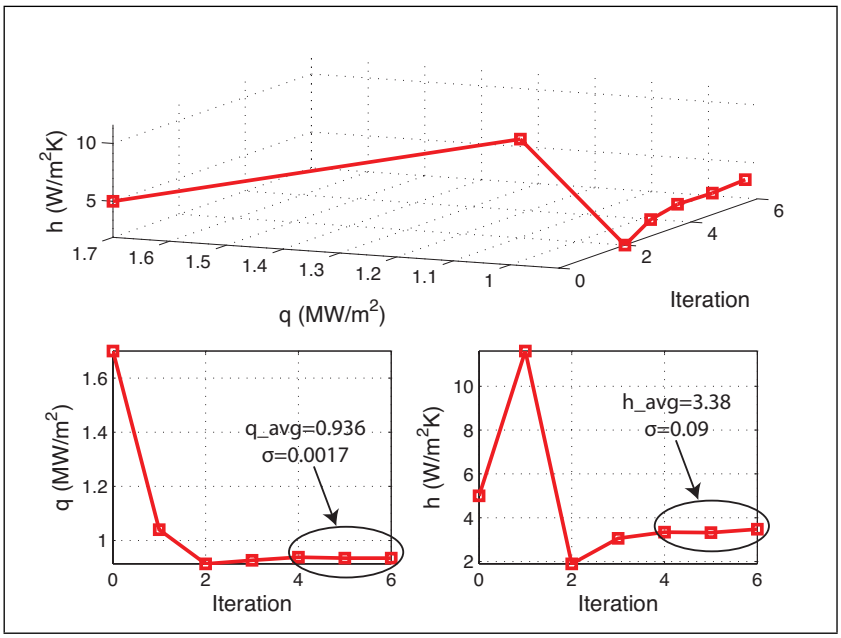

Figure 6. Least squares convergence.

tistical moments were computed from the last three iterations. Results are similar for all three methods. The least squares method used the least amount of wall time and memory of the three methods. Wall time for each iteration, independent of recomputing the COMSOL® model for the updated parameters, was approximately two orders of magnitude longer for extended information filter and four orders of magnitude longer for extended Kalman filter than the wall time for least squares. Memory usage was approximately 1.5 times more for extended information filter and 2 times more for extended Kalman filter than the memory required by least squares. When considering convergence behavior and computational cost, least squares outperforms the other methods for this type of parameter identification.

Figure 8 compares the temperature response measured during the experiment with the temperature response of the model using $q'' = 0.930\,\mathrm{MW/m^2}$ and $h = 3.20\,\mathrm{W/m^2\,K}$. The residuals [27, 28] are illustrated in Figure 9. Agreement between the model and the experiment is acceptable, however improvement could be achieved through modifications to the heating profile (e.g., secondary heating). Agreement with the experiment is better when simultaneously estimating q'' and h than when estimating q'' with h arbitrarily fixed. A check of the boundary effect errors (not illustrated) was conducted to ensure the plate was sized sufficiently large. Of particular interest is in the region of ($\pm 4\,\mathrm{cm}$,$\pm 4\,\mathrm{cm}$) where the errors remain well below 0.5% for the entire experiment. Even at ($\pm 10\,\mathrm{cm}$,$\pm 10\,\mathrm{cm}$), the errors are below 1% for much of the experiment and stay below 3% for the entire experiment. Solution sensitivity analysis was performed to find $q\partial T/\partial q$ and $h\partial T/\partial h$ versus time using finite differences (Figures 10 and 11). These figures indicate that q'' dominates the solution. Although q'' and h appear not to be correlated, since the sensitivity to h is much smaller ($< 10\%$) than the sensitivity to q'', estimating both parameters simultaneously is difficult.

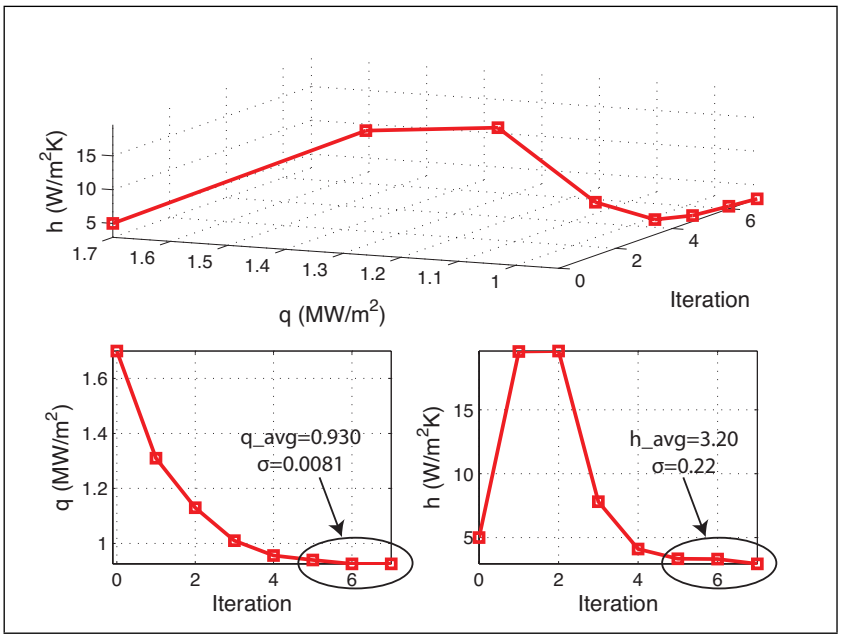

Figure 7. Extended Kalman filter and extended information filter convergence. The filters produce identical results and are presented together.

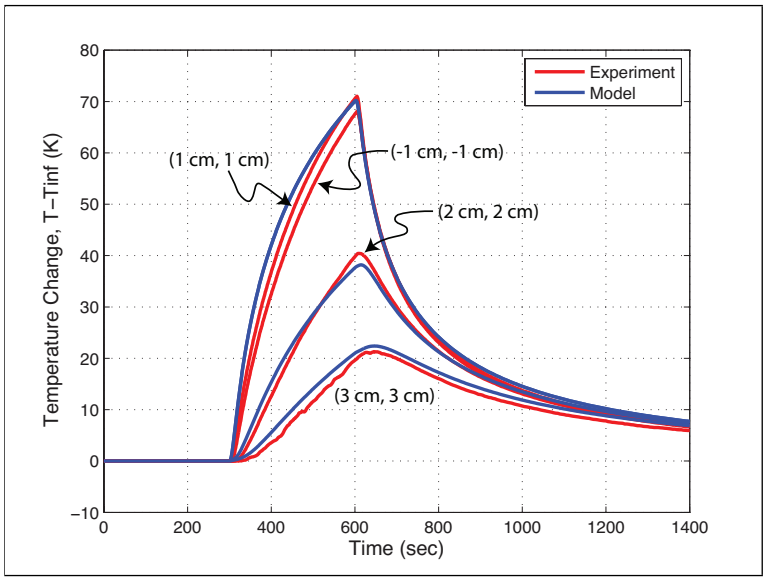

Figure 8. Comparison of theTemperature response on non-heated side of the plate at four sensor locations.

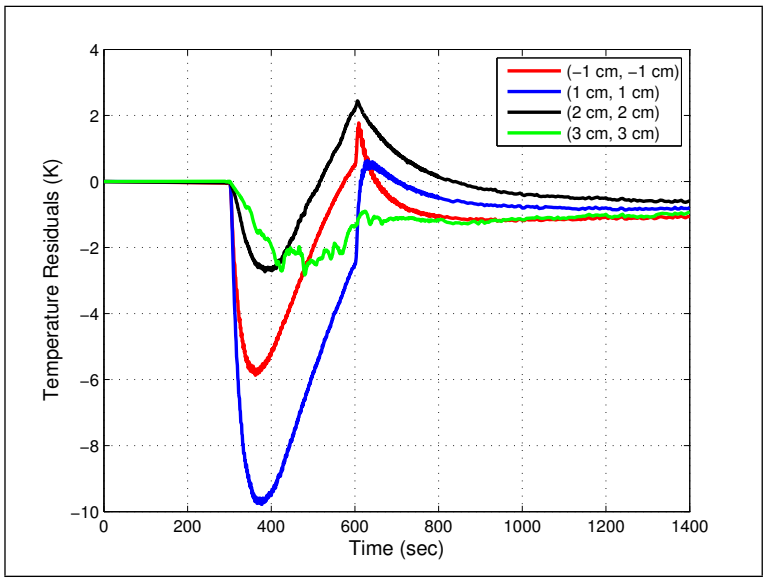

Figure 9. Residuals of the model when compared to the experiment measurements on the non-heated side.

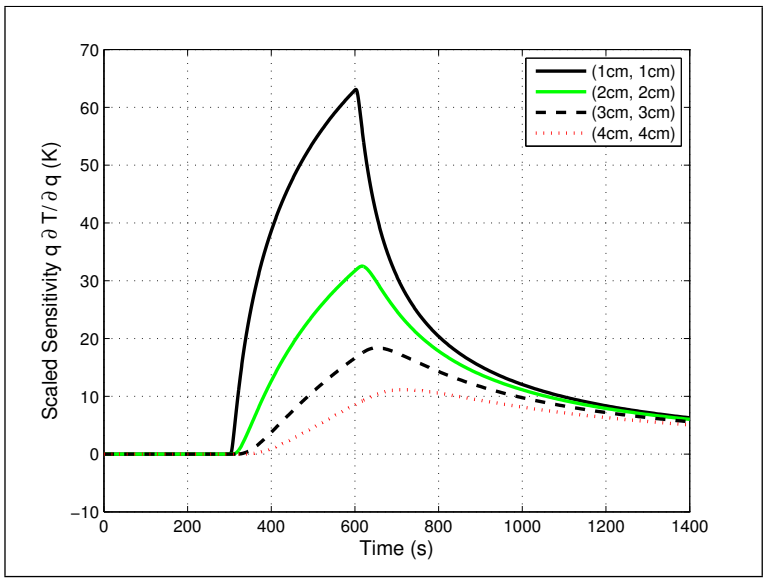

Figure 10. Heat flux sensitivity.

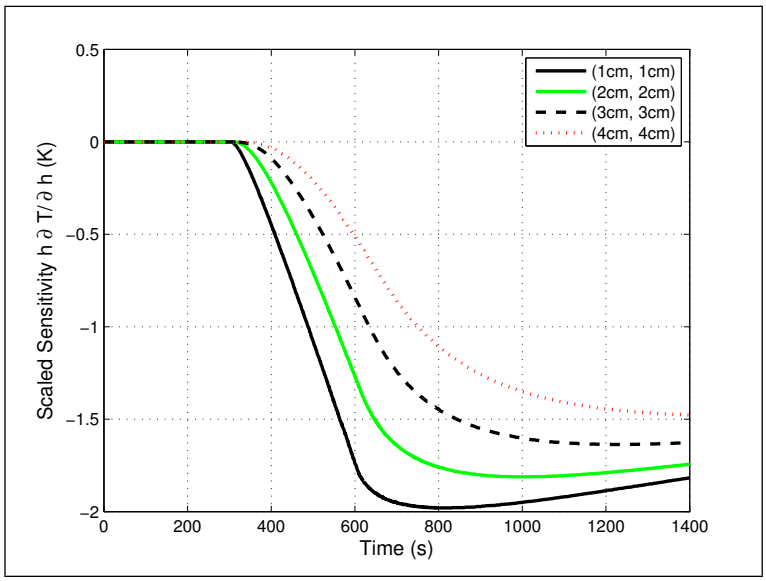

Figure 11. Convection coefficient sensitivity.

5. Heating Source Localisation

Locating and characterising a heating source depends upon many factors such as heating source movements in time, heating source magnitude changes in time, and other transient behaviours. Fairly restrictive assumptions can be imposed that simplify the problem. Analysis and algorithm development can proceed using these restrictive assumptions and then assumptions can be relaxed in stages to achieve the end result of source localisation and characterisation. The assumptions for this work are:

(1) Source in fixed position (location unknown)
(2) Source applied at time $t = 300\,\mathrm{s}$ and removed at $t = 600\,\mathrm{s}$
(3) $q'' = 0.930\,\mathrm{MW/m^2}$ over $0.00635\,\mathrm{m}$ diameter circular area while source applied (value obtained in parameter identification above)
(4) Secondary heating is characterised by a Gaussian with magnitude $q''_g = 100\,\mathrm{W/m^2}$ and variance $\sigma_g^2 = 0.0009\,\mathrm{m^2}$ while source applied
(5) Convection coefficient $h = 3.20\,\mathrm{W/m^2K}$ on both sides of the plate (value obtained in parameter identification above)
(6) Convection coefficient $h = 3\,\mathrm{W/m^2K}$ on the plate edges
(7) Thermal conductivity $k = 15\,\mathrm{W/mK}$
(8) Specific heat $C_p = 500\,\mathrm{J/kgK}$ and density $\rho = 8,000\,\mathrm{kg/m^3}$
(9) Positions of sensors are ($\pm 4\,\mathrm{cm}$, $\pm 4\,\mathrm{cm}$) on the non-heated side

The following six measurement models have been identified for analysis:

(1) Temperature measurement model
(2) Radius from temperature measurement model
(3) Ultrasonic pulse-echo time of flight measurement model
(4) Radius from ultrasonic pulse-echo time of flight measurement model
(5) Ultrasonic pulse one-way time of flight measurement model
(6) Ellipse from ultrasonic one-way pulse time of flight measurement model

These measurement models represent different ways to collect measurements (sensors) and different ways to process the data. Two measurement models are

based on thermocouple sensors and four models are based on ultrasonic transducer sensors. Comparison of the six measurement models is performed using the extended Kalman filter (algorithm in Table 2) to locate the source (x_q, y_q). For all six measurement models, the estimated state is $X_t = [x_s, y_s]^T$ where x_s and y_s represent the estimated location of the source at time t. There is no input to the state thus the state model is $a = I_2$ and the state Jacobian is $A = I_2$. Sensitivity of the state variance was compared for values from $\sigma^2 = 0.01\,\mathrm{m}^2$ to $0.000001\,\mathrm{m}^2$ with the lower values providing a damping effect. A state variance of $\sigma^2 = 0.0001\,\mathrm{m}^2$ provides a good compromise between damping and stability and will be used for all measurement model comparisons in this work. Thus, the state covariance matrix is $Q_t = 0.0001\,\mathrm{m}^2 * I_2$, where I_2 is a 2×2 identity matrix.

5.1. Temperature Measurement Model

In this direct model, temperatures are measured using four thermocouples on the non-heated side of the plate. Expected temperatures and the partial derivatives are obtained directly from COMSOL® to form the measurement transition function $b(\overline{X}_t)$ and the Jacobian B_t.

$$b(\overline{X}_t) = \begin{bmatrix} \overline{\theta}_1 \\ \overline{\theta}_2 \\ \overline{\theta}_3 \\ \overline{\theta}_4 \end{bmatrix} \tag{5}$$

$$B_t = \begin{bmatrix} -\frac{\partial \overline{\theta}_1}{\partial x_1} & -\frac{\partial \overline{\theta}_1}{\partial y_1} \\ -\frac{\partial \overline{\theta}_2}{\partial x_2} & -\frac{\partial \overline{\theta}_2}{\partial y_2} \\ -\frac{\partial \overline{\theta}_3}{\partial x_3} & -\frac{\partial \overline{\theta}_3}{\partial y_3} \\ -\frac{\partial \overline{\theta}_4}{\partial x_4} & -\frac{\partial \overline{\theta}_4}{\partial y_4} \end{bmatrix} \tag{6}$$

where t is time in seconds with a time step of 1 s, $\overline{\theta}$ is the expected change in temperature relative to a reference, obtained from COMSOL®, if the heating source is located at (x_s, y_s), and (x_i, y_i) with $i = 1, 2, 3, 4$ indicating the locations of the four thermocouples. The Jacobian B_t is constructed using the derivatives with respect to sensor position for convenience since this information can be obtained with one COMSOL® simulation. The derivatives are obtained directly from COMSOL®. Based on the flat plate experiment above, sensor noise is assumed be $\pm 0.045\,\mathrm{K}$ and is normally distributed ($\sigma^2 = (0.045/3)^2 = 2.225 \times 10^{-4}\,\mathrm{K}^2$). The measurement covariance matrix is $R = 2.225 \times 10^{-4}\,\mathrm{K}^2 * I_4$.

5.2. Radius From Temperature Measurement Model

This indirect model is similar to the previous model in that temperatures are measured using thermocouples, but in this model, COMSOL® is used as a lookup table to convert measured temperatures to a radius from each sensor to the source. Knowledge of the heating start time, one of the assumptions in this work, enables a simple COMSOL® lookup of expected temperatures for a range of radius values from the heating source. Linear interpolation is used with this lookup table to obtain an expected radius for each temperature measurement.

$$r_i = \sqrt{(x_i - x_s)^2 + (y_i - y_s)^2} \tag{7}$$

where (x_i, y_i) is the location of sensor i for $i = 1, 2, 3, 4$ and (x_s, y_s) the heating source location. The Jacobian is based solely on geometry, which may reduce errors.

$$\begin{aligned}\frac{\partial r_i}{\partial x_s} =& \frac{1}{2}\left((x_i - x_s)^2 + (y_i - y_s)^2\right)^{-\frac{1}{2}} \\ & \left(\frac{\partial}{\partial x_s}(x_i^2 - 2x_i x_s + x_s^2)\right)\end{aligned} \tag{8}$$

$$\frac{\partial r_i}{\partial x_s} = \frac{x_s - x_i}{r_i}, \frac{\partial r_i}{\partial y_s} = \frac{y_s - y_i}{r_i} \tag{9}$$

The measurement transition function $b(\overline{X}_t)$ and the Jacobian B_t are then

$$b(\overline{X}_t) = \begin{bmatrix} \sqrt{(x_1 - x_s)^2 + (y_1 - y_s)^2} \\ \sqrt{(x_2 - x_s)^2 + (y_2 - y_s)^2} \\ \sqrt{(x_3 - x_s)^2 + (y_3 - y_s)^2} \\ \sqrt{(x_4 - x_s)^2 + (y_4 - y_s)^2} \end{bmatrix} \tag{10}$$

$$B_t = \begin{bmatrix} \frac{x_s - x_1}{r_1} & \frac{y_s - y_1}{r_1} \\ \frac{x_s - x_2}{r_2} & \frac{y_s - y_2}{r_2} \\ \frac{x_s - x_3}{r_3} & \frac{y_s - y_3}{r_3} \\ \frac{x_s - x_4}{r_4} & \frac{y_s - y_4}{r_4} \end{bmatrix} \tag{11}$$

where t is time in seconds with a time step of 1 s, $\overline{r}_i$ with $i = 1, 2, 3, 4$ is the radius from the sensor to the source, obtained from COMSOL®, if the source is located at (x_s, y_s), and (x_i, y_i) with $i = 1, 2, 3, 4$ indicating the locations of the four thermocouples. Based on the flat plate experiment above, sensor noise is assumed be ± 0.045 K and is normally distributed ($\sigma^2 = (0.045/3)^2 = 0.000225\,\mathrm{K}^2$). Since measured temperature is being related to radius, sensor noise must be converted into radius noise. The complication in this conversion arises from the fact that radius is a non-linear function of temperature and time. Based on insights gained from the forward conduction model and analysis of the temperature response in the plate, a value of 0.015 m/K was used resulting in a radius noise of ± 0.000675 m with normal distribution ($\sigma^2 = 5.06 \times 10^{-8}\,\mathrm{m}^2$). The measurement covariance matrix, therefore, is $R = 5.06 \times 10^{-8}\,\mathrm{m}^2 * I_4$.

5.3. Ultrasonic Pulse-echo Time of Flight Measurement Model

This direct model uses ultrasonic pulses to measure the average temperature through the material thickness at each sensor location. In the pulse-echo method, the ultrasonic pulse travels through the material thickness, reflects off the boundary, and returns to the transducer. The time of flight is [29, 30]

$$G_{ii} = \frac{2L}{v_o}\left(1 + \xi\theta_{avg}\big|_0^L\right) \tag{12}$$

where L represents the material thickness, v_0 is the speed of sound in the material at a reference temperature, ξ is the ultrasonic time of flight factor which is material dependent, and θ is the change in temperature from the reference temperature. The ultrasonic pulse time of flight measurement model consists of obtaining expected temperatures from COMSOL®, computing the average temperature between the transducer and the boundary, and then computing an expected time of flight using equation 12 to form the measurement transition function $b(\overline{X}_t)$ (equation 13). The Jacobian partial derivatives are obtained using time of flight difference when moving the source in the x and y directions independently (equation 14).

$$b(\overline{X}_t) = \begin{bmatrix} \overline{G}_1 \\ \overline{G}_2 \\ \overline{G}_3 \\ \overline{G}_4 \end{bmatrix} \tag{13}$$

$$B_t = \begin{bmatrix} -\frac{\partial \overline{G}_1}{\partial x_1} & -\frac{\partial \overline{G}_1}{\partial y_1} \\ -\frac{\partial \overline{G}_2}{\partial x_2} & -\frac{\partial \overline{G}_2}{\partial y_2} \\ -\frac{\partial \overline{G}_3}{\partial x_3} & -\frac{\partial \overline{G}_3}{\partial y_3} \\ -\frac{\partial \overline{G}_4}{\partial x_4} & -\frac{\partial \overline{G}_4}{\partial y_4} \end{bmatrix} \tag{14}$$

where t is time in seconds with a time step of 1 second, $\overline{G}_i$ with $i = 1, 2, 3, 4$ is the expected ultrasonic pulse time of flight, obtained from COMSOL®, with the heating source at location (x_s, y_s), and (x_i, y_i) with $i = 1, 2, 3, 4$ indicating the locations of the four transducers. The Jacobian B_t is constructed using the derivatives with respect to sensor position for convenience since this information can be obtained with one COMSOL® simulation. The derivatives are obtained from COMSOL® using finite differences by independently varying the x and y positions of all sensors by 0.0001 m. Based on the flat plate experiment above, sensor noise is assumed be $\pm 2.3 \times 10^{-10}$ s and is normally distributed ($\sigma^2 = 5.88 \times 10^{-21}\,\text{sec}^2$). The measurement covariance matrix, therefore, is $R = 5.88 \times 10^{-21}\,\text{sec}^2 * I_4$.

5.4. Radius From Ultrasonic Pulse-echo Time of Flight Measurement Model

In this indirect model, ultrasonic pulse-echo time of flight is measured using four transducers on the non-heated side of the plate. Similar to radius from temperature method, this method converts the measured time of flight to a radius using the COMSOL® model as a lookup table. Knowledge of the heating start time, one of the assumptions in this work, enables a simple COMSOL® lookup of expected temperatures for a range of radius values from the heating source. Temperatures in the plate are related to time of flight through equation 12. Linear interpolation is used with this lookup table to obtain an expected radius for each time of flight measurement. Equations 7 to 9 develop the geometry behind the measurement

transition function $b(\overline{X}_t)$ and the Jacobian B_t which are

$$b(\overline{X}_t) = \begin{bmatrix} \sqrt{(x_1 - x_s)^2 + (y_1 - y_s)^2} \\ \sqrt{(x_2 - x_s)^2 + (y_2 - y_s)^2} \\ \sqrt{(x_3 - x_s)^2 + (y_3 - y_s)^2} \\ \sqrt{(x_4 - x_s)^2 + (y_4 - y_s)^2} \end{bmatrix} \tag{15}$$

$$B_t = \begin{bmatrix} \frac{x_s - x_1}{r_1} & \frac{y_s - y_1}{r_1} \\ \frac{x_s - x_2}{r_2} & \frac{y_s - y_2}{r_2} \\ \frac{x_s - x_3}{r_3} & \frac{y_s - y_3}{r_3} \\ \frac{x_s - x_4}{r_4} & \frac{y_s - y_4}{r_4} \end{bmatrix} \tag{16}$$

where t is time in seconds with a time step of 1 second, $\overline{r}_i$ with $i = 1, 2, 3, 4$ is the radius from the sensor to the source, obtained from COMSOL®, if the source is located at (x_s, y_s), and (x_i, y_i) with $i = 1, 2, 3, 4$ indicating the locations of the four thermocouples. Based on the flat plate experiment above, sensor noise is assumed be $\pm 2.3 \times 10^{-10}$ s and is normally distributed ($\sigma^2 = 5.88 \times 10^{-21}\,\mathrm{sec}^2$). Sensor noise in terms of temperature can be expressed as

$$\theta_{noise} = \frac{G_{noise} v_0}{2L\xi} = 0.84\,\mathrm{K} \tag{17}$$

Since measured time of flight is being related to radius, sensor noise must be converted into radius noise. The complication in this conversion arises from the fact that radius is a non-linear function of time of flight and time. Based on insights gained from the forward conduction model and analysis of the temperature response in the plate, a value of 0.015 m/K was used resulting in a radius noise of ± 0.0126 m with normal distribution ($\sigma^2 = 1.76 \times 10^{-5}\,\mathrm{m}^2$). The measurement covariance matrix, therefore, is $R_t = 1.76 \times 10^{-5}\,\mathrm{m}^2 * I_4$.

5.5. *Ultrasonic Pulse One-way Time of Flight Measurement Model*

Instead of sending an ultrasonic pulse through to a boundary and receiving the echo at the original transducer, one transducer can transmit the pulse and another transducer can receive the pulse. The time of flight is

$$G_{ij} = \frac{R_{ij}}{v_o}\left(1 + \xi \theta_{avg}|_i^j\right) \tag{18}$$

where R_{ij} is the distance between transducers (m). This direct measurement model consists of obtaining expected temperatures from COMSOL®, computing the average temperature between the transducers, and then computing an expected time of flight to form $a(U_t, X_{t-1})$ (equation 19). For the current analysis, the average temperature is based on the line on the plate surface between the two sensors. The Jacobian partial derivatives are obtained using time of flight difference when

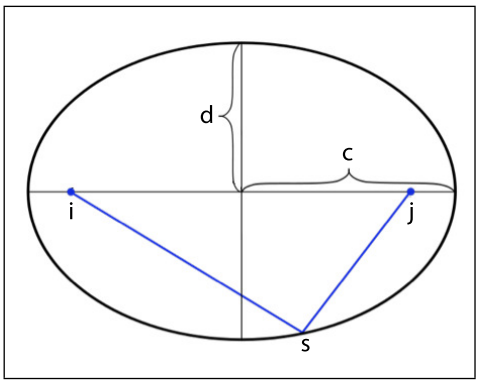

Figure 12. Ellipse properties.

moving the source in the x and y directions independently (equation 20).

$$b(\overline{X}_t) = \begin{bmatrix} \overline{G}_1 \\ \overline{G}_2 \\ \overline{G}_3 \\ \overline{G}_4 \end{bmatrix} \tag{19}$$

$$B_t = \begin{bmatrix} -\frac{\partial \overline{G}_1}{\partial x_1} & -\frac{\partial \overline{G}_1}{\partial y_1} \\ -\frac{\partial \overline{G}_2}{\partial x_2} & -\frac{\partial \overline{G}_2}{\partial y_2} \\ -\frac{\partial \overline{G}_3}{\partial x_3} & -\frac{\partial \overline{G}_3}{\partial y_3} \\ -\frac{\partial \overline{G}_4}{\partial x_4} & -\frac{\partial \overline{G}_4}{\partial y_4} \end{bmatrix} \tag{20}$$

where t is time in seconds with a time step of 1 s, $\overline{G}_i$ with $i = 1, 2, 3, 4$ is the ultrasonic pulse time of flight, obtained from COMSOL®, with the heating source located at (x_s, y_s), and (x_i, y_i) with $i = 1, 2, 3, 4$ indicating the locations of the four transducers. The Jacobian B_t is constructed using the derivatives with respect to sensor position for convenience since this information can be obtained with one COMSOL® simulation. The derivatives are obtained from COMSOL® using finite differences by independently varying the x and y positions of all sensors by 0.0001 m. Based on the flat plate experiment above, sensor noise is assumed be $\pm 1.05 \times 10^{-8}$ s and is normally distributed ($\sigma^2 = ((1.05 \times 10^{-8})/3)^2 = 1.225 \times 10^{-17}\,\text{sec}^2$). The measurement covariance matrix, therefore, is $R = 1.225 \times 10^{-17}\,\text{sec}^2 * I_4$.

5.6. Ellipse From Ultrasonic Pulse One-way Time of Flight Measurement Model

In this indirect model, a particular ultrasonic pulse time of flight at a particular time after the heater is turned on means that the source could be anywhere on an assumed elliptical shape around the sensors. Figure 12 illustrates the geometry of an ellipse. The two sensors are assumed to be the focus points for the ellipse. Since the distance between sensors is known, ellipse parameters c and d can be related to each other and the ellipse can be represented with just one parameter c.

$$r_{is} + r_{js} = 2c = \sqrt{r_{ij}^2 + 4d^2} \tag{21}$$

where i and j are sensors and s is heat source.

$$c = \frac{1}{2}\sqrt{r_{ij}^2 + 4d^2} = \frac{r_{is} + r_{js}}{2} \tag{22}$$

$$r_{is} = \sqrt{(x_i - x_s)^2 + (y_i - y_s)^2} \tag{23}$$

$$r_{js} = \sqrt{(x_j - x_s)^2 + (y_j - y_s)^2} \tag{24}$$

$$\frac{\partial c_i}{\partial x_s} = \frac{1}{2}\left[\frac{x_s - x_i}{r_{is}} + \frac{x_s - x_j}{r_{js}}\right] \tag{25}$$

$$\frac{\partial c_i}{\partial y_s} = \frac{1}{2}\left[\frac{y_s - y_i}{r_{is}} + \frac{y_s - y_j}{r_{js}}\right] \tag{26}$$

The parameter c is measured indirectly by first measuring the one-way ultrasonic pulse time of flight. The forward conduction solution is used to get time of flight for a range of c values and interpolated using the spline method to obtain c for the measured time of flight. The measurement transition function $b(\overline{X}_t)$ and the Jacobian B_t are then

$$b(\overline{X}_t) = \begin{bmatrix} c_1 \\ c_2 \\ c_3 \\ c_4 \end{bmatrix} \tag{27}$$

$$B_t = \begin{bmatrix} \frac{\partial c_1}{\partial x_s} & \frac{\partial c_1}{\partial y_s} \\ \frac{\partial c_2}{\partial x_s} & \frac{\partial c_2}{\partial y_s} \\ \frac{\partial c_3}{\partial x_s} & \frac{\partial c_3}{\partial y_s} \\ \frac{\partial c_4}{\partial x_s} & \frac{\partial c_4}{\partial y_s} \end{bmatrix} \tag{28}$$

where t is time in seconds with a time step of 1 s, c_i with $i = 1, 2, 3, 4$ is the ellipse parameter if the source is located at (x_s, y_s). Based on the flat plate experiment above, sensor noise is assumed be $\pm 1.05 \times 10^{-8}$ s and is normally distributed ($\sigma^2 = 1.22 \times 10^{-17}\,\mathrm{sec}^2$). The sensor noise in terms of temperature can be expressed as

$$\theta_{noise} = \frac{G_{noise} v_0}{L\xi} = 6.09\,\mathrm{K} \tag{29}$$

Since measured time of flight is being related to the ellipse parameter c, sensor noise must be converted into ellipse parameter noise. The complication in this conversion arises from the fact that c is a non-linear function of time of flight and time. Based on insights gained from the forward conduction model and analysis of the temperature response in the plate, a value of 0.015 m/K was used resulting in an ellipse noise of $\pm 2.04e - 4$ m for the c parameter with normal distribution ($\sigma^2 = 4.62 \times 10^{-9}\,\mathrm{m}^2$).

5.7. *Extended Kalman Filter Convergence Behaviour*

Extended Kalman filter convergence behaviour for all six measurement models are compared in Figures 13 through 16. With the heating source located inside the sensor grid (Figure 13), all measurement models converge to the correct location,

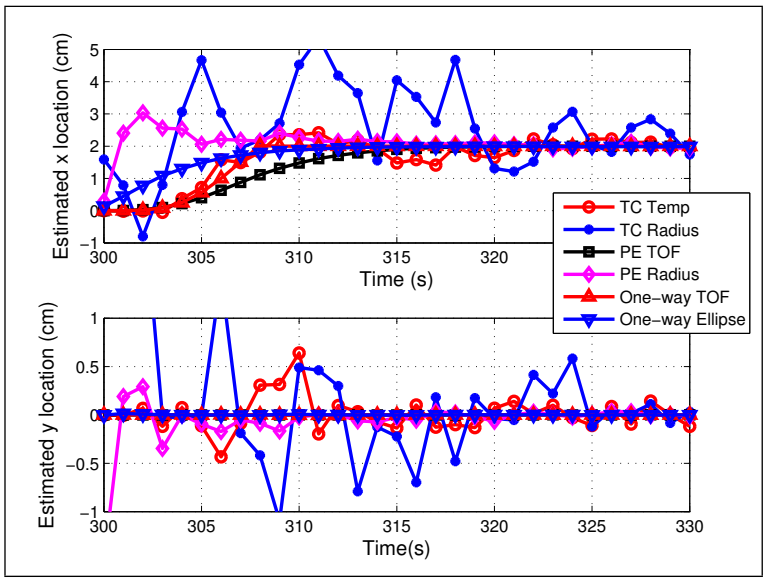

Figure 13. Extended Kalman filter convergence for all six measurement models with source at (2 cm, 0 cm) and initial guess of (0 cm, 0 cm).

however both temperature measurement models exhibit rather noisy convergence. The ellipse from ultrasonic pulse one-way time of flight measurement model produces the best results with the heating source located inside the sensor grid. With the heating source located at the edge of the sensor grid (Figure 14), all measurement models once again converge to the correct location and both temperature measurement models and the radius from ultrasonic pulse-echo time of flight measurement model exhibit undesirable convergence behaviour. The ellipse from ultrasonic pulse one-way time of flight measurement model produces the best results with the heating source located at the edge the sensor grid. With the heating source located outside of the sensor grid (Figure 15), none of the measurement models converge to the correct location, however the ellipse from ultrasonic pulse one-way time of flight and radius from ultrasonic pulse-echo time of flight measurement models converge to within 1 cm of the actual location. These examples started with an initial guess of (0 cm, 0 cm) for the heating source location. Figure 16) illustrates the convergence behaviour for all six models using an initial guess of (8 cm, 8 cm) for the heating source located inside the sensor grid. Interestingly, all direct models fail to converge to the correct location in this scenario. Overall, the ellipse from ultrasonic pulse one-way time of flight measurement model produces the best results when considering accuracy of converged solution, ability to converge to the correct solution given different initial guesses, and smoothness of convergence behaviour.

Because we are using numerical tools to solve the governing equations, we lack a set of state equations and cannot determine the observability index in the standard fashion. We can, however, examine sensitivity to heating source location relative to sensor location as well as sensitivity to other parameters including heating source magnitude, plate thermal conductivity, and plate surface convection coefficient. Sensitivity analysis to address observability is not included here and will be published separately.

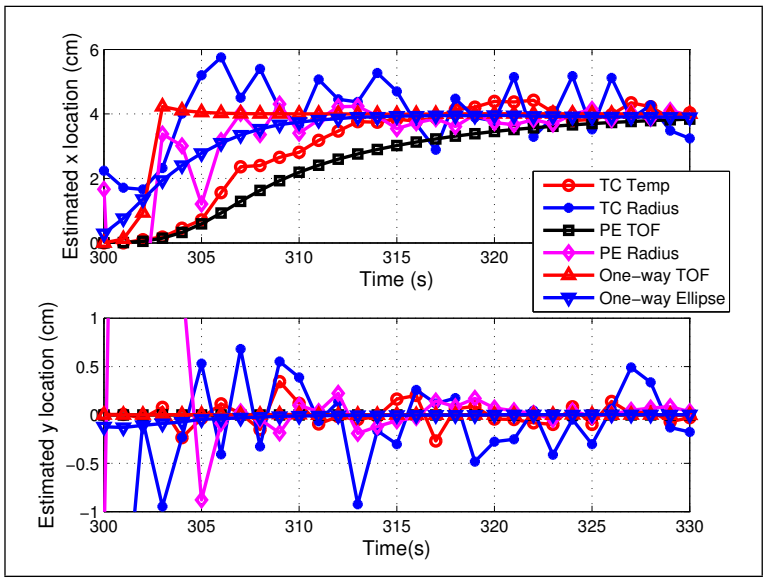

Figure 14. Extended Kalman filter convergence for all six measurement models with source at (4 cm, 0 cm) and initial guess of (0 cm, 0 cm).

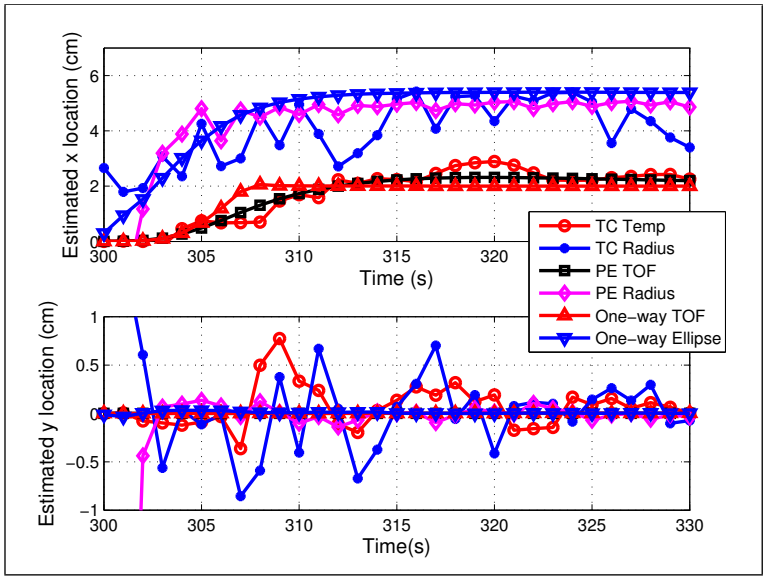

Figure 15. Extended Kalman filter convergence for all six measurement models with source at (6 cm, 0 cm) and initial guess of (0 cm, 0 cm).

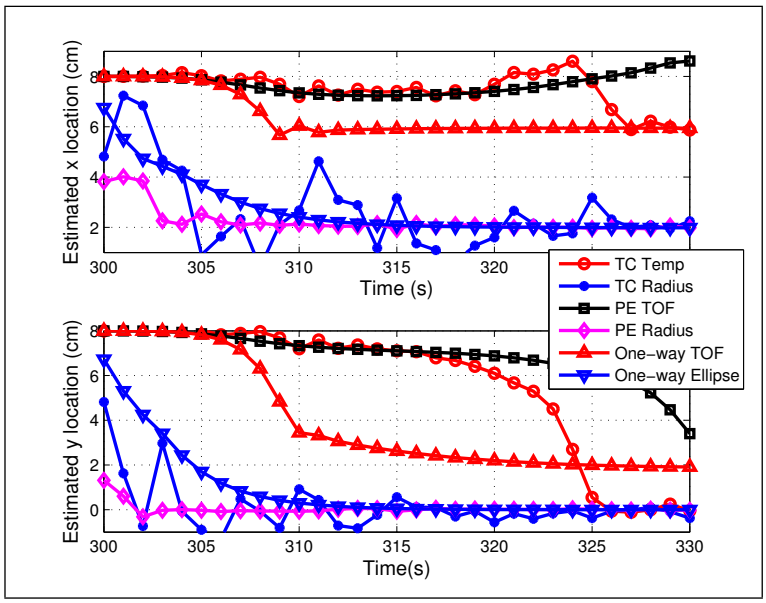

Figure 16. Extended Kalman filter convergence for all six measurement models with source at (2 cm, 0 cm) and initial guess of (8 cm, 8 cm).

6. Conclusions

Results were presented from forward conduction solution development, flat plate experimentation with a known heat source, and parameter identification of heat flux and convection coefficient on the plate. Least squares, extended Kalman filter, and extended information filter inversion methods produce similar results. This finding is significant as future work will add more free parameters (e.g., secondary heating profile) and heat source localisation to the inverse procedure. The extended Kalman filter convergence behaviour was compared using six measurement models. The ellipse from ultrasonic pulse one-way time of flight measurement model produces the best results when considering accuracy of converged solution, ability to converge to the correct solution given different initial guesses, and smoothness of convergence behaviour. Whereas this work had no inputs to the state model, the ability to add inputs to a recursive state estimator (e.g., a Gaussian filter) is anticipated to be more robust for heat source localisation and in turn for boundary layer transition localisation and characterisation.

Nomenclature

A	state Jacobian
a	state model;
B	measurement Jacobian
b	expected measurement
C	heat capacity (J/K)
c_p	specific heat (J/kg K)
c	distance from ellipse center to ellipse edge along the major axis
d	distance from ellipse center to ellipse edge along the minor axis
F	cumulative density function
G	ultrasonic time of flight (s)

$\overline{G}$	expected ultrasonic time of flight (s)
h	convection heat transfer coefficient (W/m^2-K)
I_n	$n \times n$ identity matrix
K	Kalman gain
k	thermal conductivity (W/m-K)
L	length (m)
l	length (m)
Nu	Nusselt Number
P	probability
Pr	Prandtl Number
p	probability
Q	heat source;
	state covariance
q''	heat flux (W/m^2)
R	measurement covariance;
	radius (m)
Ra	Rayleigh Number
r	radius (m)
$\overline{r}$	expected radius (m)
S	sensitivity
T	temperature (K)
t	time (s)
U	control input
v	sound speed (m/s)
w	width (m);
	particle weight
X	state
$\overline{X}$	predicted state
x, y, z	rectangular coordinates (m)
$\overline{x}, \overline{y}$	predicted rectangular coordinates (m)
Z	actual measurements

Greek Letters

α	thermal diffusivity (m^2/s)
γ	temperature dependence of Young's modulus (1/K)
Δ	normalized temperature difference
∇	Laplacian operator
δ	coefficient
θ	temperature change relative to reference (K)
$\overline{\theta}$	predicted temperature change relative to reference (K)
κ	thermal conductivity (W/m-K)
ξ	ultrasonic time of flight temperature factor (1/K)
ρ	density (kg/m^3)
Σ	covariance
$\overline{\Sigma}$	predicted covariance
σ^2	variance for a Gaussian probability density function
τ	period (s)

ϕ	information vector
$\overline{\phi}$	predicted information vector
Ω	information matrix
$\overline{\Omega}$	predicted information matrix

Subscripts

0	initial or zero point
amb	ambient
i	sensor
inf	infinity
j	sensor
g	Gaussian profile
q	heat source
s	heat source
T	temperature
t	time (s)
ts	time-scaling coefficient

β	state parameters vector

Acknowledgements

The authors would like to acknowledge the financial support from the Brazilian agency Conselho Nacional de Desenvolvimento Científico e Tecnológico (CNPq), the United States Air Force Office of Scientific Research (AFOSR), and the United Stated Air Force Research Laboratory (AFRL). The authors would also like to acknowledge Dr. Mitch Wilkes, Associate Professor of Electrical Engineering and Associate Professor of Computer Engineering at Vanderbilt University for his assistance in understanding recursive state estimation and Dr. Don Yuhas, Industrial Measurement Systems, Inc. for his guidance through experimentation and analysis challenges.

References

[1] H.L. Reed, R.L. Kimmel, S. Schneider, D. Arnal, and W. Saric, *Drag Prediction and Transition in Hypersonic Flow*, in *Symposium on Sustained Hypersonic Flight, AGARD Conference on Future Aerospace Technology in the Service of the Alliance*, Palaiseau, France, 14–17 Apr, NATO Research and Technology Organisation, Palaiseau, France, 1997.

[2] T.J. Horvath, S.A. Berry, and B.R. Hollis, *Boundary Layer Transition on Slender Cones in Conventional and Low Disturbance Mach 6 Wind Tunnels*, in *32nd AIAA Fluid Dynamics Conference and Exhibit*, AIAA-2002-2743, St. Louis, MO, 24–27 Jun, AIAA, St. Louis, MO, 2002.

[3] S. Schneider, *Flight data for boundary-layer transition at hypersonic and supersonic speeds*, Journal of Spacecraft and Rockets 36 (1999), pp. 8–20.

[4] S. Schneider, *Hypersonic laminar-turbulent transition on circular cones and scramjet forebodies*, Progress in Aerospace Sciences 40 (2004), pp. 1–50.

[5] K. Berger, S. Rufer, R. Kimmel, and D. Adamczak, *Aerothermodynamic Characteristics of Boundary Layer Transition and Trip Effectiveness of the HIFiRE Flight 5 Vehicle*, in *AIAA Proceedings*, AIAA-2009-4055, June, , 2009.

[6] S. Thrun, W. Burgard, and D. Fox *Probabilistic Robotics*, The MIT Press, Cambridge, MA, 2006.

[7] J. Frankel, M. Keyhani, B. Elkins, and R. Arimilli, *New In Situ Method for Estimating Thermal Diffusivity Using Rate-Based Temperature Sensors*, Journal of Thermophysics and Heat Transfer 24 (2010), pp. 811–817.

[8] C. Pullins and T. Diller, *In situ High Temperature Heat Flux Sensor Calibration*, International Journal of Heat and Mass Transfer 53 (2010), pp. 3429–3438.

[9] D. Walker, E. Scott, and R. Nowak, *Estimation methods for two-dimensional conduction effects of shock-shock heat fluxes*, Journal of Thermophysics and Heat Transfer 14 (2000), pp. 533–539.

[10] M. Yu, G. Sarner, C.C.M.Luijten, M. Alden, R. Baert, and L. Goeyde , *Survivability of thermographic phosphors (YAG:Dy) in a combustion environment*, Measurement Science and Technology 21 (2010), p. 037002.

[11] T. Liu, Z. Cai, J. Lai, J. Rabal, and J.P. Sullivan, *Analytical Method for Determining Heat Flux from Temperature-Sensitive-Paint Measurements in Hypersonic Tunnels*, Journal of Thermophysics and Heat Transfer 24 (2010), pp. 1–10.

[12] G. Gauffre, *Détection de la transition laminaire turbulent par thermographie infrarouge (Detection of laminar-turbulent transition by infrared thermography)*, La Recherche Aérospatiale (1988), pp. 11–22.

[13] L. Lynnworth and E. Papadakis, *Ultrasonic Thermometry*, in *Ultrasonics Symposium*, San Francisco, CA, 21–23 Oct, IEEE, San Francisco, CA, 1970.

[14] H.N.G. Wadley, S.J. Norton, F. Mauer, B. Droney, E.A. Ash, and C.M. Sayers, *Ultrasonic Measurement of Internal Temperature Distribution*, Philosophical Transactions of the Royal Society of London. Series A, Mathematical and Physical Sciences 320 (1986), pp. 341–361.

[15] H.A. Tasman, H.E. Schmidt, J. Richter, M. Campana, and G. Fayl, *Treson experiments: Measurement of temperature profiles in nuclear fuels by means of ultrasonic thermometers*, High Temperatures - High Pressures 9 (1977), pp. 387–406.

[16] M. Konno, A. Cui, N. Nishiwaki, and S. Hori, *Measurement of the polymer melt temperature in injection molding machine by using ultrasonic technique*, in *proceedings of the 51st Annual Technical Conference, Society of Plastics Engineers*, New Orleans, LA, USA, 1993, pp. 2798–2803.

[17] B.S. Hoyle and S.P. Luke, *Ultrasound in the process industries*, Engineering Science and Education Journal 3 (1994), pp. 119–122.

[18] B.G.W. Yee and J.C. Couchman, *Application of ultrasound to NDE of materials*, IEEE Transactions on Sonics and Ultrasonics SU-23 (1976), pp. 299–305.

[19] J. Moll, R. Schulte, B. Hartmann, C.P. Fritzen, and O. Nelles, *Multi-site damage localization in anisotropic plate-like structures using an active guided wave structural health monitoring system*, Smart Materials and Structures 19 (2010), p. 045022.

[20] X.P. Zhu, P. Rizzo, A. Marzani, and J. Bruck, *Ultrasonic guided waves for nondestructive evaluation/structural health monitoring of trusses*, Measurement Science and Technology 21 (2010), p. 045701.

[21] M. Majji, J.N. Juang, and J.L. Junkins, *Observer/Kalman-Filter Time-Varying System Identification*, Journal of Guidance, Control, and Dynamics 33 (2010), pp. 887–900.

[22] D.P. Bertsekas, *Incremental least squares methods and the extended Kalman filter*, SIAM Journal on Optimization 6 (1996), pp. 807–822.

[23] M.R. Myers, A.B. Jorge, M.J. Mutton, and D.G. Walker, *High heat flux point source sensitivity and localization analysis for an ultrasonic sensor array*, International Journal of Heat and Mass Transfer 55 (2012), pp. 2472–2485.

[24] V. Kozlov, V. Adamchik, and V. Lipovtsev, *Local heating of an unbounded orthotropic plate through a circular and annular domain*, Journal of Engineering Physics and Thermophysics 57 (1989), pp. 1381–1391.

[25] F.P. Incropera and D.P. DeWitt *Introduction to Heat Transfer*, 4th John Wiley and Sons, Hoboken, NJ, 2002.

[26] K.A. Woodbury, *Sequential function specification method using future times for function estimation*, in *Inverse Engineering Handbook*, , in *Inverse Engineering Handbook*, ed. K.A. WoodburyK.A. Woodbury ed., CRC Press, Boca Raton, FL, 2003.

[27] J. Beck and K. Woodbury, *Inverse problems and parameter estimation: integration of measurements and analysis*, Measurement Science and Technology 9 (1998), pp. 839–847.

[28] K.J. Dowding and B.F. Blackwell, *Sensitivity Analysis for Nonlinear Heat Conduction*, Journal of Heat Transfer 123 (2001), p. 1.

[29] M.R. Myers, D.G. Walker, D.E. Yuhas, and M.J. Mutton, *Heat flux determination from ultrasonic pulse measurements*, in *International Mechanical Engineering Congress and Exposition*, IMECE2008-69054, Boston, MA, 2–6 Nov, ASME, 2008.

[30] M.R. Myers, D.G. Walker, D.E. Yuhas, and M.J. Mutton, *Heat flux determination from ultrasonic pulse measurements*, International Journal of Heat and Mass Transfer (in review, 2010) (in review).